Article

Novel Method for the Arsenic Removal Experiment and Mechanism Analysis

Hao Zhu,* Wenhui Lin, and Liwen Fan

Read Online

ACCESS | Metrics & More | Article Recommendations

ABSTRACT: This study focuses on the hydrothermal synthesis of magnetically activated carbon and its efficacy in As(III) adsorption. The successful incorporation of magnetite nanoparticles within the porous carbon structure was confirmed, enriching the adsorbent's properties. Comprehensive characterization was performed to analyze the pore size distribution, zeta potential at varying pH levels, and thermostability using thermogravimetric analysis. These adsorbents exhibited high As(III) removal efficiency with a uniform pore distribution. The zeta potentials were observed to decrease with an increase in pH, suggesting a relationship between adsorbent charge and pH. Adsorption dynamics were rigorously modeled using pseudo-first-order, pseudo-second-order, Elovich, and intraparticle diffusion models for different adsorbents labeled as *a*, *b*, *c*, and *d*. Each adsorbent displayed unique fitted parameters, revealing varied adsorption capabilities. The study further explored the adsorption kinetics and found that the pseudo-second-order kinetics model and the Langmuir model were most appropriate for describing the adsorption process. Adsorption thermodynamics was also fitted to elucidate the underlying adsorption mechanisms. For the *a, b, c*, and *d* adsorbents, the pseudo-first-order model, the $q_{e\ (cal)}$ values for the four adsorbents were 434.2, 418.4, 283.5, and 279.5 $\mu g/g$, respectively. Take adsorbent *a* as an example; the q_m values for 298, 303, 308, and 313 K were 702, 673, 605, and 589 $\mu g/g$, respectively, and K_L values of these temperatures were 0.021, 0.031, 0.018, and 0.009 L/μg, respectively. For the Langmuir model, the R^2 values at the four temperatures were 0.999, 0.978, 0.985, and 0.993, respectively, which indicated that the Langmuir model showed higher fitness. For the Freundlich model, the K_L values (L/μg) at the parameters of these temperatures are 432, 409, 328, and 294, respectively. For the Freundlich model, the $1/n$ values at temperatures of 298, 303, 308, and 313 K are 0.049, 0.045, 0.052, and 0.035, respectively. For the Freundlich model, the R^2 values at parameters of 298, 303, 308, and 313 K are 0.986, 0.989, 0.982, and 0.872, respectively. For the Temkin model, the B values (in J/mol) are 30.93, 0.894, 0.824, and 0.782 at these temperatures, respectively. The K_T values (in L/μg) are 1.02×10^6, 0.07×10^6, 0.003×10^6, and 0.002×10^6, respectively. The R^2 values are 0.973, 0.958, 0.972, and 0.894, respectively. In the end, the ΔH, ΔS, and ΔG values for different adsorbents were calculated. Collectively, these findings contribute significant insights into the design and application of magnetically activated carbon adsorbents for effective As(III) removal.
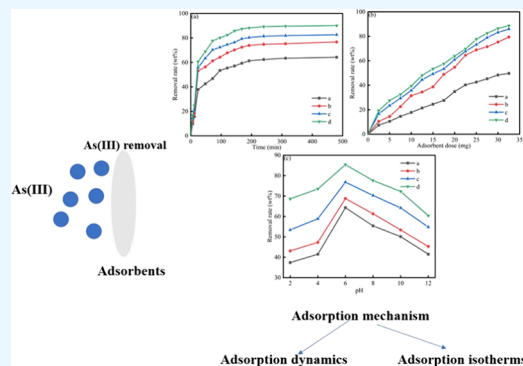
1. INTRODUCTION

Approximately 68% of the freshwater resources utilized by humans on earth are derived from groundwater. Despite this, significant regions worldwide are experiencing issues with arsenic contamination in groundwater due to the progression of industrialization and natural causes. As a major water quality concern, arsenic pollution has become an escalating problem.[1,2]

Arsenic is considered one of the most potent metallic pollutants within our water resources.[3] Its harmful characteristics include being nondegradable and nonvolatile, which presents an ongoing threat to human health. Even in minute concentrations, arsenic poses a severe risk.[4] The toxic dose of arsenic in humans is estimated to be around 10−52 mg, whereas the lethal dose ranges between 60 and 200 mg. The origins of arsenic in groundwater can be traced back to two

primary sources: human activities and natural occurrences.[5] Human activities contribute to the rise in groundwater arsenic levels both directly and indirectly, primarily through the extraction of arsenic-containing minerals, the use of arsenic-infused insecticides in agricultural irrigation, and the release of arsenic-laden wastewater.[5−7] Arsenic from these sources gradually infiltrates groundwater through sedimentation and

natural precipitation processes, leading to arsenic contamination.[8]

The rapid growth of the industrial sector has significantly heightened the problem of freshwater pollution, a crucial issue worldwide. This pollution primarily stems from toxic metals such as lead, cadmium, mercury, nickel, chromium, tin, zinc, manganese, copper, and, notably, arsenic.[9,10] These hazardous metals can provoke acute and chronic diseases when their concentrations surpass safe limits. Arsenic, inherently present in the earth's crust, exists in both organic and inorganic forms in our environment. The natural sources of arsenic are primarily due to shifts in natural environmental conditions, which can trigger the release of arsenic from arsenic-containing minerals.[11,12] This arsenic can bind to the surface of absorptive rocks, thereby increasing the concentration of arsenic in groundwater.[13] These formation mechanisms are the main contributors to the increasing levels of arsenic in groundwater.[14,15]

Given the heightened mobility, toxicity, and fluidity of As(III) compared to As(V), and the fact that As(III) typically exists in molecular form, the removal efficiency of various processes for As(III) is considerably lower than for As(V).[16] Therefore, to effectively remove As(III) from water, most treatment processes necessitate its oxidation to a more treatable form, As(V). This oxidation method is both relatively simple and cost-effective, composed primarily of air oxidation and chemical oxidation.[17] Nonetheless, chemical oxidation and its control process require stringent management. Due to the limitations of aeration or the addition of pure oxygen in rapidly and efficiently preoxidizing As(III) to As(V), chemical oxidants are often introduced. These commonly include $KMnO_4$, Fenton reagents, O_3, Cl_2, H_2O_2, etc.[18] However, in treating drinking water, it is crucial to avoid the generation of toxic byproducts from residual oxidants.[19] Hence, during the actual operation, appropriate catalysts are often selected to encourage the oxidation process.

An increase in public awareness of the arsenic content in water, its quality, and associated health risks has become a matter of global concern.[20] Among these, the adsorption method is preferred due to its efficiency, simplicity, scalability, and ability to reduce health risks.[21] Natural and synthetic adsorbents in use encompass activated alumina, hybrid nanomaterials, transition metal oxides, and ceramic adsorbents.[22−24]

It is favored for its abundant pore structure, surface functional groups, cost-effectiveness, scalability, and high arsenic adsorption capacity.[12,25] For instance, Europe produces around 500,000 t of onion waste annually. This study, therefore, aims to convert such onion waste into highly porous activated carbon products using various activators and temperature regimes.[26,27] The resulting activated carbon exhibits a highly mesoporous structure with an expansive surface area. Incorporating magnetite into this porous framework further improves the arsenic removal efficiency of the activated carbon.

This study represents the first known application of magnetized activated carbon derived from onion waste for the removal of As(III). Our work's significant contribution is two-fold: it enhances industrial synergies by converting waste into a value-added product, and it provides valuable insights for researchers and manufacturers involved in developing cost-effective and eco-friendly arsenic removal technologies.

2. MATERIALS AND METHODS

2.1. Materials. All the chemicals, As_2O_3 (99.9%), NaOH (99%), $(NH_4)_6Mo_7O_{24} \cdot 4H_2O$ (99.9%), HNO_3 (65%), HCl (37%,), H_2SO_4 (97%), NH_4OH (33%), KIO_3 (99.5%), $FeCl_2 \cdot 4H_2O$ (98%), $FeCl_3 \cdot 6H_2O$ (99%), $C_6H_8O_6$ (99.5%), H_3PO_4 (85%), and $C_8H_4K_2O_{12} - Sb_2 \cdot 3H_2O$ (99%), were analytical grade and from Aladdin Reagent Co., Ltd., Shanghai, China.

2.2. Onion Pretreatment and Carbonization. Onions acquired from a local market were thoroughly rinsed to eliminate any dust or dirt. These onions were then dried overnight in a sand bath at 110 °C. The dried onions were crushed and ground to achieve a uniform particle size. The processed onion material was subjected to pyrolysis at 450 °C under a nitrogen flow rate of 0.2 L/min for 1 h. Following this, the sample was submerged in distilled water until the pH reached 7 and then dried overnight at 110 °C.

2.3. Carbon Activation Using Different Activators. The carbon produced in Section 2.1 was divided into four equal portions and activated with different activating agents, namely,@ HNO_3, H_3PO_4, CH_3COOH, and NaOH. Each portion was immersed overnight in the respective activator solution. These activated carbon samples were then heated in a tubular furnace at 600 °C for 1 h under a steady nitrogen flow rate of 0.2 L/min. Postactivation, the samples were rinsed with distilled water until a pH of 7 was achieved and then dried overnight at 110 °C. The activated samples were designated as *a,b,c*, and *d*, based on the activator used.

2.4. Magnetization of Activated Carbon. Each sample was magnetized by immersion in Fe_3O_4 using the solvothermal method. This process involved mixing 0.149 g of $FeCl_2 \cdot 4H_2O$ and 0.405 g of $FeCl_3 \cdot 6H_2O$ salts in 120 mL of distilled water for 15 min. Then, 10 mL of hydrochloric acid was added followed by the introduction of 1 g of the activated carbon sample. The precipitate, NH_4OH, was added to the solution, and the contents were transferred to a high-voltage autoclave lined with Teflon. The autoclave was heated at 180 °C for 2 h. This procedure was repeated for each of the carbon samples. Finally, the samples were rinsed with distilled water until the pH reached approximately 7. The magnetized samples were named as *a,b,c*, and *d*.

2.5. As(III) Determination in the Aqueous Systems Using the Colorimetric Method. A standard solution (100 mg/L) was prepared by dissolving 0.132 g of As_2O_3 in 20 mL of 1 M sodium hydroxide. To neutralize the pH, 50 mL of 0.5 M hydrochloric acid was added. The volume of the solution was then adjusted to 1000 mL using high-purity water. The resulting solution was stored in brown bottles to prevent oxidation. Different concentrations of stock solutions were prepared from this standard solution for further analysis. The colorimetric analysis was performed by preparing a mixture containing 4 mL of 10.8% ascorbic acid and 4 mL of 0.56% ammonium molybdate solution followed by the addition of 6 mL of molybdenum. It has been found that this mixture stabilizes within 3 h at temperatures below 30 °C. To enhance the formation of complex anions and zirconium molybdenum, As(III) was oxidized to As(V). This was achieved by dissolving KIO_3 in hydrochloric acid to prepare a 2 mM KIO_3 solution. Then, 0.5 mL of this solution was added to 5 mL of each As(III) solution at various concentrations. The solution underwent ultrasonic treatment at room temperature until complete oxidation of As(III) to As(V) was achieved.
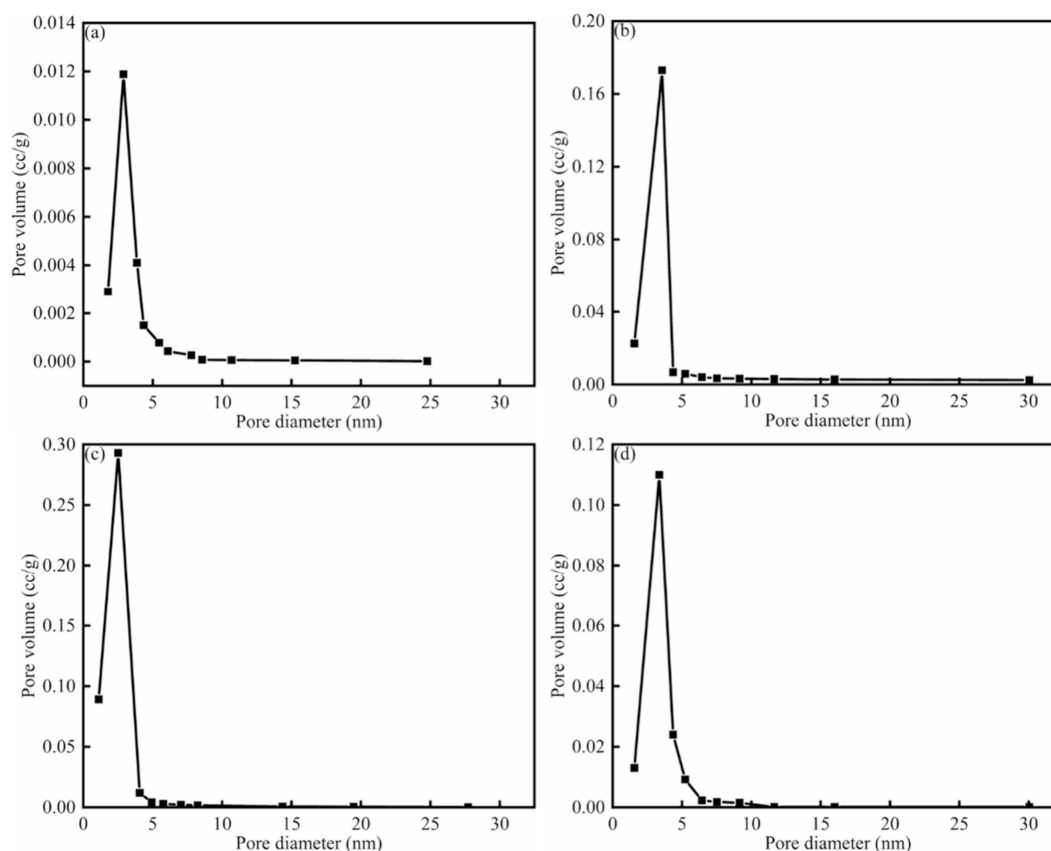
Figure 1. Pore size distribution curve for the (a) *a*, (b) *b*, (c) *c*, and (d) *d* adsorbent.

Following the ultrasonic treatment, 0.5 mL of the reagent was added to each bottle containing solutions of different As(III) concentrations. The mixture was gently stirred and allowed to rest for 30 min to form complex blue anions and arsenic molybdates. The UV-visible spectrum for each sample was scanned and recorded in the wavelength range of 400−1100 nm. A calibration curve was obtained using an absorbance peak at 900 nm, and a linear equation was derived from this curve to determine unknown arsenic concentrations.

2.6. Adsorption Study. The effectiveness of the adsorbent was evaluated under optimal conditions, which included time, adsorbent dosage, and pH. For each concentration and temperature effect, 10 mg of the adsorbent was added to a series of vials, each containing a different concentration of As(III) solution at pH 7. The vials were then placed in a shaker bath operating at 130 rpm for 4 h. Following this period, filtration was carried out immediately to cease contact between the adsorbent and the As(III) solution. The filtrate was then analyzed using the colorimetric method. The amount of adsorption and the percentage of removal were calculated.

The time required to reach equilibrium was optimized using kinetic adsorption studies. Vials were prepared, each containing 10 mL of 1000 μg/L As(III) solution, with 10 mg of the adsorbent added to each vial. The vials were placed in a shaker bath operating at 130 rpm at 298 K, and samples were taken at various intervals from 5 to 360 min. After each interval, one vial was removed from the shaker bath and the solution was filtered. The filtrate was then analyzed as previously described, and the adsorption at time t and the removal percentage at different time intervals were calculated.

Simultaneously, to examine the effect of the amount of adsorbent, a series of samples were prepared, each containing 10 mL of 1000 μg/L As(III) solution, with varying amounts of adsorbent added to each vial. These vials were then placed in a shaker bath at 298 K with a shaking speed of 130 rpm for 4 h. Following this, the solution was filtered and subjected to colorimetric analysis as mentioned above. The concentration and removal rate of As(III) were then calculated.

Last, to study the impact of pH, a series of vials, each containing 10 mL of 1000 μg/L As(III) solution, were prepared and the pH of each solution was adjusted within the range of 2−10. The adsorption process was carried out at 298 K with a shaking speed of 130 rpm for 4 h.

3. RESULTS AND DISCUSSION

3.1. Pore Size Distribution Curve. Figure 1 shows the pore size distribution curve for different adsorbents. The pore size distribution curve corroborates the appearance of widened hysteresis loops, signifying a substantial presence of mesopores. Open loops were noted in porous vessels with narrow openings, indicating that the adsorbent is not easily compromised. All the peak values for different pore sizes were lower than 5 nm.

3.2. Zeta Potential. The data show that the adsorbents display positive charges when the pH is below their individual IEP (isoelectric point) and negative charges when it is above. The IEP values for different adsorbents were different, as illustrated in Figure 2. When the pH values increased, the zeta potentials would decrease.

3.3. TG Analysis. The TG analysis for different adsorbents is shown in Table 1. For adsorbent *a*, the initial decomposition
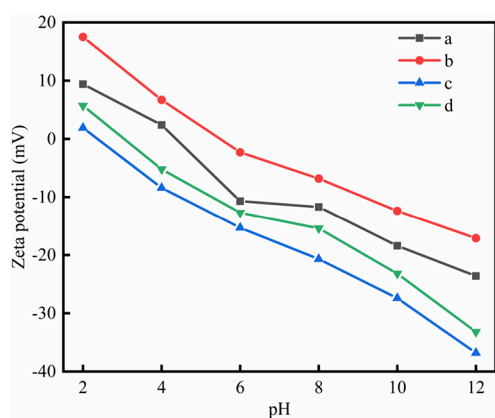
Figure 2. Zeta potentials of different adsorbents.

Table 1. TG Analysis for Different Adsorbents

adsorbent	T_1 (°C)	weight loss (wt %)	T_2 (°C)	weight loss (wt %)	total weight loss (wt %)
a	371	3.4	864	4.5	7.9
b	432	4.5	933	5.7	10.2
c	464	5.3	968	8.4	13.7
d	533	5.9	1023	9.5	15.4

temperature (T_1) was 371 °C, the initial weight loss was 3.4 wt %, the second decomposition temperature (T_2) was 864 °C, the second weight loss was 4.5 wt %, and the total weight loss was 7.9 wt %. For *b*, *c*, and *d* adsorbents, the T_1 temperatures were 432, 464, and 533 °C, respectively. The corresponding weight losses were 4.5, 5.3, and 5.9 wt %, respectively. The T_2 temperatures were 933, 968, and 1023 °C, respectively. The corresponding weight losses were 5.7, 8.4, and 9.5 wt %,

respectively. The total weight losses were 10.2, 13.7, and 15.4 wt %, respectively. The different adsorbents showed different thermal stabilities. For different adsorbents, the initial decomposition temperature and second decomposition temperature were different.

3.4. Optimization of Process Conditions. To optimize the parameters affecting the arsenic adsorption efficiency of various adsorbents, the impact of different variables was explored.[28,29] Figure 3 shows the time, adsorbent dose (mg), and pH effect on the As(III) removal rate. As shown in Figure 3a, the removal rate of As(III) adsorption increased when the time increased, and when the time increased to 180 min, the As(III) adsorption would remain stable. The reason was due to the fact that for the initial time, the corresponding adsorption site was not saturated, and therefore the corresponding adsorption would increase suddenly. When the adsorption time was the same, the adsorption effect followed the rules that *a* < *b* < *c* < *d*. The graph clearly demonstrates the consistent and seamless adsorption of As(III) across all adsorption surfaces up to the saturation point, suggesting a single-surface coverage.

Figure 3b illustrates the impact of the adsorbent dosage on the As(III) removal rate. The results indicated that the As(III) removal rate increased with the increase in adsorbent dose, and when the adsorbent dose was nearly 30 mg, the corresponding As(III) removal would become stable.

Figure 3c shows the pH effect on the As(III) removal rate. The results showed that the average pH value significantly influenced the surface charge and ionization of the adsorbent, thereby affecting its absorption capacity. When the pH was lower than 6, the As(III) removal rate would increase with the increase in pH, and then the As(III) removal rate would decrease when the pH was higher than 6. The reason was due
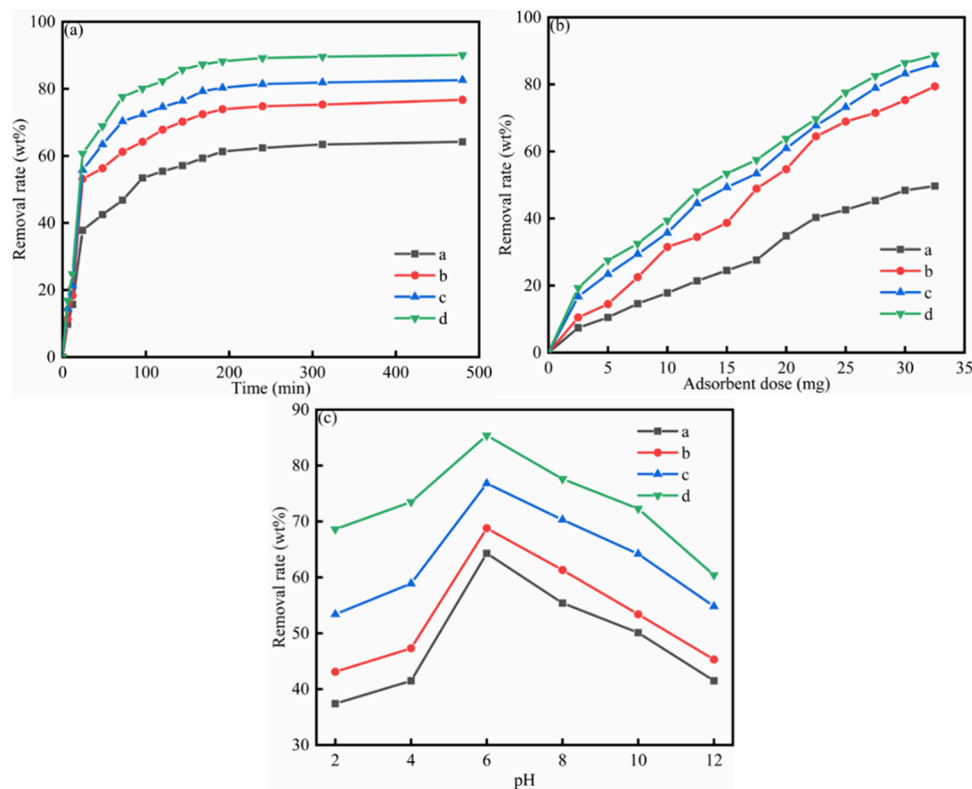

Figure 3. (a) Time, (b) adsorbent dose (mg), and (c) pH effect on the As(III) removal rate.

to the fact that the higher pH would be beneficial to the As(III) adsorption, but when the pH increased, the corresponding As(III) adsorption would decrease because the adsorption was monolayer adsorption.

The reasons for the decrease in the removal percentage in the second and third stages were as follows. Saturation of active sites: During the initial stage, the maximum number of active sites on the magnetic activated carbon is available for arsenic adsorption. As the process progresses, many of these active sites get occupied, resulting in fewer sites available for subsequent arsenic ions, which can lead to a decrease in removal percentage in the later stages.

Readsorption phenomenon: As the concentration of arsenic ions in the solution decreases (due to initial adsorption), there could be a possibility of a readsorption phenomenon where the adsorbed arsenic ions might reenter the solution, slightly decreasing the overall removal percentage. Competitive adsorption: If there are other species or contaminants present in the solution, then they might compete with arsenic ions for the active sites on the adsorbents, especially as the major portion of arsenic gets adsorbed in the initial stages. Diffusion limitations: In the initial stages, the concentration gradient between the arsenic ions in the solution and the adsorbent surface is high, leading to faster diffusion rates. However, as the process progresses and the gradient reduces, the diffusion rate might decrease, resulting in slower adsorption and a lower removal percentage. Changes in pH: The pH of the solution can vary during the adsorption process. As the stages progress, slight variations in pH could influence the ionization state of arsenic and its interaction with the adsorbents, leading to varying removal percentages.

3.5. Kinetic Modeling. Understanding the time required for the system to reach equilibrium is critical in assessing the feasibility of the adsorption process.[30] Owing to mass transfer phenomena, the adsorption system does not instantly reach equilibrium. Kinetic adsorption studies involve observing the time progression during the adsorption process to acquire concentration distributions over time.[31,32] Adsorption at the solid–liquid interface represents phenomena that primarily include physical adsorption or chemical adsorption of these particles. Our objective was to gain a deeper understanding of the distinct properties of activated carbon adsorption by employing various models.

The pseudo-first-order kinetic model was applied during the adsorption period following diffusion or physical adsorption. The pseudo-first-order kinetic model was as follows:

$$\ln(q_e - q_t) = \ln q_e - k_1 t \tag{1}$$

This relation can be used to calculate the adsorption capacity Q $(\mu g/g)$. However, a regression coefficient of less than 0.90 indicates that the pseudo-first-order model may not be adequate for describing the adsorption of As(III) on magnetically activated carbon.

The pseudo-second-order kinetic model is commonly used to explain adsorption dynamics. This model can predict behavior across the entire adsorption spectrum and views surface complexation as a decrease in the rate step. In this model, adsorption depends on the availability of unoccupied adsorption sites rather than on the concentration of the adsorbate, and the reaction rate depends on the amount of adsorbate on the surface. The pseudo-second-order model is represented as follows:

$$\frac{t}{q_t} = \frac{1}{k_2 q_e^2} + \frac{t}{q_e} \tag{2}$$

The Elovich model, a kinetic model that assumes heterogeneous surface energy, provides a comprehensive understanding of the adsorption kinetics of chemical species. This model presumes that the adsorption rate decreases consistently with increasing adsorbate concentration. The Elovich model in its linear form can be expressed as follows:

$$q_t = \frac{1}{\beta}\ln(\alpha\beta) + \frac{1}{\beta}\ln t \tag{3}$$

The initial adsorption rate, represented by the intercept value α, and the chemical adsorption activation energy, represented by β, can be calculated using this model. Moreover, the intraparticle diffusion model can also be applied to the experimental data to discern the adsorption mechanism, as shown in eq 4.

$$q_t = k_{id}t^{1/2} + C_i \tag{4}$$

Table 2 shows the kinetic parameters for different adsorbents by the pseudo-first-order model. The results

Table 2. Kinetic Parameters for Different Adsorbents by the Pseudo-First-Order Model

kinetic parameters	a	b	c	d
K_1 (min^{-1})	0.0301	0.030	0.031	0.028
$q_{e\ (cal)}$ $(\mu g/g)$	434.2	418.4	283.5	279.5
$q_{e\ (exp)}$ $(\mu g/g)$	1162	902	862	821
R^2	0.753	0.929	0.7842	0.6832
RMSE	0.80923	0.5832	0.9934	0.8274
reduced Chi-Squared	0.70421	0.310323	0.92842	0.87492

indicated that the R^2 values for c and d adsorbents were high, but for a and b adsorbents, the values were low, which indicated that the pseudo-first-order model was not suitable for a and b adsorbents. In addition, the $q_{e\ (cal)}$ $(\mu g/g)$ values for these four adsorbents a, b, and c, and d were 434.2, 418.4, 283.5, and 279.5, respectively. For the kinetic parameters, the $q_{e\ (exp)}$ values for adsorbents of classes a, b, and c, and d were 1162, 902, 862, and 821, respectively. The corresponding R^2 values for these adsorbent classes were 0.753, 0.929, 0.7842, and 0.6832. The RMSE values for adsorbents of classes a, b, c, and d were 0.80923, 0.5832, 0.9934, and 0.8274, respectively. The reduced Chi-Squared values for these adsorbent classes were 0.70421, 0.310323, 0.92842, and 0.87492. Table 3 shows the kinetic parameters for different adsorbents by the pseudo-second-order model, and the results indicated that R^2 values were high for different adsorbents, which indicated that the pseudo-second-order model was suitable for the corresponding adsorption dynamics. For the kinetic parameters, the K_2 (min^{-1}) values in adsorbents of classes a, b, and c, and d were 1.81×10^{-4}, 2.49×10^{-4}, 3.21×10^{-4}, and 3.01×10^{-4} min^{-1}, respectively. The $q_{e\ (cal)}$ $(\mu g/g)$ values in $\mu g/g$ for these adsorbent classes were 1209, 903, 903, and 901. The $q_{e\ (exp)}$ $(\mu g/g)$ values in $\mu g/g$ were 1082, 872, 862, and 848. The corresponding R^2 values for these adsorbents were 0.9475, 0.9382, 0.999, and 0.997. The RMSE values for these classes were 0.00431, 0.00102, 0.02319, and 0.01921. The reduced

Table 3. Kinetic Parameters for Different Adsorbents by the Pseudo-Second-Order Model

kinetic parameters	a	b	c	d
K_2 (min^{-1})	1.81×10^{-4}	2.49×10^{-4}	3.21×10^{-4}	3.01×10^{-4}
$q_{e\ (cal)}$ (ug/g)	1209	903	903	901
$q_{e\ (cal)}$ (ug/g)	1082	872	862	848
R^2	0.9475	0.9382	0.999	0.997
RMSE	0.00431	0.00102	0.02319	0.01921
reduced Chi-Squared	4.982×10^{-4}	1.392×10^{-4}	7.130×10^{-2}	6.531×10^{-2}

Chi-Squared values were 4.982×10^{-4}, 1.392×10^{-4}, 7.130×10^{-2}, and 6.531×10^{-2}.

Tables 4 and 5 show the kinetic parameters for different adsorbents by the Elovich model and intraparticle diffusion

Table 4. Kinetic Parameters for Different Adsorbents by the Elovich Model

kinetic parameters	a	b	c	d
β (g/μg)	0.0213	0.009	0.014	0.009
α (μg/g min)	3.52×10^{10}	35,892	7.25×10^{10}	6.85×10^{10}
R^2	0.7842	0.8024	0.8579	0.8035
RMSE	10.8241	34.832713	18.903538	17.563663
reduced Chi-Squared	114.294	1383.902	363.783	354.753

Table 5. Kinetic Parameters for Different Adsorbents by the Intraparticle Diffusion Model

kinetic parameters	a	b	c	d
C_i	1008.4	613.92	721.83	718.35
K_{id} (μg/g min$^{1/2}$)	9.7382	15.903	6.8923	6.4782
R^2	0.7092	0.7832	0.6923	0.5735
RMSE	19.924	79.934	28.942	27.582
reduced Chi-Squared	519.903	5998.382	829.934	819.924

model, respectively, and the R^2 values were low, which indicated that the two models had drawbacks. In Table 4, for the kinetic parameters, the β values for adsorbents of classes *a, b, c,* and *d* were 0.0213, 0.009, 0.014, and 0.009 g/μg, respectively. The α values for these adsorbent classes were 3.52×10^{10}, 35,892, 7.25×10^{10}, and 6.85×10^{10} μg/g min. The corresponding R^2 values for these adsorbents were 0.7842, 0.8024, 0.8579, and 0.8035. The RMSE values for these classes were 10.8241, 34.832713, 18.903538, and 17.563663. The reduced Chi-Squared values for these adsorbent classes were 114.294, 1383.902, 363.783, and 354.753. In Table 5, for the kinetic parameters, the C_i values for adsorbents of classes *a, b, c,* and *d* were 1008.4, 613.92, 721.83, and 718.35, respectively. The K_{id} values for these adsorbent classes were 9.7382, 15.903, 6.8923, and 6.4782 μg/g min$^{1/2}$. The corresponding R^2 values for these adsorbents were 0.7092, 0.7832, 0.6923, and 0.5735. The RMSE values for these classes were 19.924, 79.934, 28.942, and 27.582. The reduced Chi-Squared values for these adsorbent classes were 519.903, 5998.382, 829.934, and 819.924.

Table 2 shows the kinetic parameters for different adsorbents by the pseudo-first-order model. The results

indicated that the R^2 values for *c* and *d* adsorbents were high, but for *a* and *b*, the values adsorbents were low, which indicated that the pseudo-first-order model was not suitable for *a* and *b* adsorbents. In addition, the $q_{e\ (cal)}$ (μg/g) values for there four adsorbents *a, b,* and *c,* and *d* were 434.2, 418.4, 283.5, and 279.5, respectively. Table 3 shows the kinetic parameters for different adsorbents by the pseudo-second-order model, and the results indicated that R^2 values were high for different adsorbents, which indicated that the pseudo-second-order model was suitable for the corresponding adsorption dynamics. Tables 4 and 5 show the kinetic parameters for different adsorbents by the Elovich model and intraparticle diffusion model, respectively, and the R^2 values were low, which indicated that the two models had drawbacks.

3.6. Adsorption Isotherms. Various methods are used to calculate adsorption capacity. The adsorption isotherm characterizes the change in adsorption capacity per unit mass of adsorbent at a constant temperature.[33−35]

When formulating various equilibrium models, the relationship between equilibrium adsorption and relevant factors was examined. The adsorption isotherm models are utilized to represent experimental data, facilitating the evaluation of adsorbent interaction efficiency. These models describe adsorption occurring uniformly with equivalent energy, signifying monolayer adsorption interactions. The Langmuir model was shown as follows:

$$q_e = \frac{q_m K_L C_e}{1 + K_L C_e} \tag{5}$$

$$\frac{C_e}{q_e} = \frac{1}{q_m K_L} + \frac{C_e}{q_m} \tag{6}$$

$$R_L = \frac{1}{1 + K_L C_0} \tag{7}$$

where K_L is the Langmuir constant related to the energy of adsorption and useful to calculate the value of R_L that can be used to predict adsorption feasibility. If $R_L > 1$ adsorption is unfavorable, then $0 < R_L$ less than 1 adsorption is favorable, and $R_L = 1$ linear adsorption, while for $R_L = 0$, adsorption is irreversible. This model adheres to the theory of adsorption, suggesting that adsorption happens directly via surface ion or covalent reactions in the formation layer.

The Freundlich equation is also derived (nonempirically) by attributing the change in the equilibrium constant of the binding process to the heterogeneity of the surface and the variation in the heat of adsorption. The Freundlich model showed an exponential relationship between the equilibrium adsorption capacity and the equilibrium concentration. The detailed Freundlich model was as follows:

$$q_e = K_f C_e^{1/n} \tag{8}$$

$$\ln q_e = \frac{1}{n}\ln C_e + \ln K_f \tag{9}$$

The Freundlich constants $1/n$ and K_f represent the adsorption strength (nonuniformity factor) and adsorption capacity, respectively. The highest value of $1/n$ increases the interaction between the adsorbate and the adsorbent. In this study, $1/n$ is less than 1, indicating the existence of favorable adsorption processes.

Table 6. Adsorption Parameters Calculated for Adsorption of As(III) by the *a* Adsorbent

model	parameters	298 K	303 K	308 K	313 K
Langmuir	q_m (μg/g)	702	673	605	589
	K_L (L/μg)	0.021	0.031	0.018	0.009
	R^2	0.999	0.978	0.985	0.993
	R_L	0.034	0.023	0.052	0.043
Freundlich	K_F (L/μg)	432	409	328	294
	$1/n$	0.049	0.045	0.052	0.035
	R^2	0.986	0.989	0.982	0.872
Temkin	B (J/mol)	30.93	0.894	0.824	0.782
	K_T (L/μg)	1.02×10^6	0.07×10^6	0.003×10^6	0.002×10^6
	R^2	0.973	0.958	0.972	0.894
Dubinin	q_m (μg/g)	756	703	653	622
	β (mol^2/kJ^2)	2.6×10^{-9}	3.3×10^{-9}	3.5×10^{-9}	2.9×10^{-9}
	E (kJ/mol)	12.12	11.34	10.67	10.25
	R^2	0.935	0.912	0.882	0.912

Table 7. Adsorption Parameters Calculated for Adsorption of As(III) by the *b* Adsorbent

model	parameters	298 K	303 K	308 K	313 K
Langmuir	q_m (μg/g)	1783	1583	998	973
	K_L (L/μg)	0.009	0.009	0.0087	0.0073
	R^2	0.987	0.953	0.975	0.998
	R_L	0.078	0.086	0.087	0.073
Freundlich	K_F (L/μg)	1008	692	472	463
	$1/n$	0.053	0.091	0.078	0.072
	R^2	0.904	0.983	0.978	0.893
Temkin	B (J/mol)	82.03	120.03	73.35	72.93
	K_T (L/μg)	0.073×10^6	0.042×10^6	0.061×10^6	0.054×10^6
	R^2	0.904	0.964	0.942	0.928

The Temkin isotherm model considers the effect of indirect adsorbate−adsorbent interaction on the adsorption process. It is based on the assumption that the heat of adsorption of all the molecules in a layer decreases linearly due to the increase in surface coverage of the adsorbent. The decrease in heat of adsorption is linear rather than logarithmic, as implied in the Freundlich isotherm. Further, the adsorption is characterized by uniform distribution of binding energies, up to a maximum binding energy. The Temkin isotherm model was shown as follows:

$$q_e = \frac{RT}{b_T}\ln(k_T C_e) \tag{10}$$

$$q_e = \frac{RT}{b_T}\ln k_T + \frac{RT}{b_T}\ln C_e \tag{11}$$

where K_T is the equilibrium binding constant (L/mol) corresponding to the maximum binding energy, b_T is related to the adsorption heat, R is the universal gas constant (8.314 J/K/mol), and T is the temperature.

The Dublin isotherm was another fitness method[36−38] that was shown as follows:

$$q_e = q_m \exp(-\beta \varepsilon^2) \tag{12}$$

$$\varepsilon = RT\ln\left(1 + \frac{1}{C_e}\right) \tag{13}$$

$$E = \frac{1}{\sqrt{2\beta}} \tag{14}$$

where q_m is the D−R monolayer capacity (mg/g), β (mol^2/kJ^2) is a constant with dimensions of energy, ε is the Polanyi sorption potential, which is the amount of energy required to pull an adsorbed molecule from its sorption site, and E is the mean free energy of adsorption per mole of the adsorbate (kJ/mol).

Table 6 shows the adsorption parameters calculated for adsorption of As(III) by the *a* adsorbent. As shown in Table 6, q_m values for 298, 303, 308, and 313 K were 702, 673, 605, and 589 μg/g, respectively. K_L values for 298, 303, 308, and 313 K were 0.021, 0.031, 0.018, and 0.009 L/μg, respectively. For the Langmuir model, the R^2 values were high. For the Freundlich model, the K_F values (in L/μg) at parameters of 298, 303, 308, and 313 K are 432, 409, 328, and 294, respectively. For the Freundlich model, the $1/n$ values at temperatures of 298, 303, 308, and 313 K are 0.049, 0.045, 0.052, and 0.035, respectively. For the Freundlich model, the R^2 values at parameters of 298, 303, 308, and 313 K are 0.986, 0.989, 0.982, and 0.872, respectively. For the Temkin model, at temperatures of 298, 303, 308, and 313 K, the B values (in J/mol) are 30.93, 0.894, 0.824, and 0.782, respectively. The K_T values (in L/μg) are 1.02×10^6, 0.07×10^6, 0.003×10^6, and 0.002×10^6, respectively. The R^2 values are 0.973, 0.958, 0.972, and 0.894, respectively.

Table 7 shows the adsorption parameters calculated for adsorption of As(III) by the *b* adsorbent. Under the Langmuir model and across parameters of 298, 303, 308, and 313 K, the adsorption capacities q_m were observed to be 1783, 1583, 998, and 973 μg/g, respectively. Concurrently, the Langmuir constant K_L recorded values of 0.009 L/μg at both 298 and 303 K followed by 0.0087 L/μg at 308 K and 0.0073 L/μg at

313 K. The coefficient of determination, R^2, remained consistently high across these temperatures. Additionally, the separation factor or equilibrium parameter R_L was found to be 0.078 at 298 K, increasing marginally to 0.086 and 0.087 at 303 and 308 K, respectively, before decreasing to 0.073 at 313 K. Utilizing the Freundlich model across parameters of 298, 303, 308, and 313 K, the Freundlich constants K_F were observed as 432, 409, 328, and 294 L/μg, respectively. Correspondingly, the heterogeneity factor, represented as $1/n$, yielded values of 0.049 at 298 K, 0.045 at 303 K, increasing to 0.052 at 308 K, and then decreasing to 0.035 at 313 K. The coefficient of determination, R^2, exhibited high consistency at the earlier parameters with values of 0.986, 0.989, and 0.982 for 298, 303, and 308 K, respectively, but noted a drop to 0.872 at 313 K. Under the Temkin isotherm model, spanning temperatures of 298, 303, 308, and 313 K, the heat of adsorption parameter, B, demonstrated values of 30.93, 0.894, 0.824, and 0.782 J/mol, respectively. Concurrently, the Temkin isotherm constant, K_T, was observed at 1.02×10^6 at 298 K, substantially dropping to 0.07×10^6 at 303 K, and then further decreasing to 0.003×10^6 and 0.002×10^6 at 308 and 313 K, respectively. The coefficient of determination, R^2, remained fairly consistent with 0.973 at 298 K, showing a slight dip to 0.958 at 303 K, rebounding to 0.972 at 308 K, and then marking a drop to 0.894 at 313 K.

Table 8 shows the adsorption parameters calculated for adsorption of As(III) by the c adsorbent. For the Langmuir

Table 8. Adsorption Parameters Calculated for Adsorption of As(III) by the c Adsorbent

model	parameters	298 K	303 K	308 K	313 K
Langmuir	q_m (μg/g)	1245	1735	1693	1583
	K_L(L/μg)	0.003	0.002	0.001	0.001
	R^2	0.894	0.982	0.738	0.683
	R_L	0.13	0.22	0.27	0.24
Freundlich	K_F (L/μg)	409	269	121	110
	$1/n$	0.129	0.209	0.255	0.231
	R^2	0.998	0.989	0.983	0.835
Temkin	B (J/mol)	178.93	274.94	272.34	264.92
	K_T (L/μg)	0.0685	0.089	0.026	0.017
	R^2	0.893	0.783	0.873	0.763

model, across the temperature range of 298, 303, 308, and 313 K, the maximum adsorption capacities (q_m) were observed to be 1245, 1735, 1693, and 1583 μg/g, respectively. In tandem, the Langmuir constants (K_L) for these temperatures showed values of 0.003, 0.002, 0.001, and 0.001 L/μg. The associated coefficients of determination (R^2) exhibited values of 0.894, 0.982, 0.738, and 0.683, while the separation factor (R_L) revealed figures of 0.13, 0.22, 0.27, and 0.24, sequentially across the parameter range. Shifting focus to the Freundlich adsorption model, the Freundlich constants (K_F) at the aforementioned parameters registered values of 409, 269, 121, and 110 L/μg. Concurrently, the heterogeneity factor ($1/n$) ranged between 0.129 and 0.231 with precise values at 0.129, 0.209, 0.255, and 0.231 for 298, 303, 308, and 313 K, respectively. Their R^2 equivalents showed notable consistencies at 0.998, 0.989, and 0.983, descending to 0.835 at 313 K. Last, under the Temkin adsorption model, the heat of adsorption parameter (B) displayed values of 178.93, 274.94, 272.34, and 264.92 J/mol, for each increasing temperature. The Temkin isotherm constant (K_T) followed a pattern of 0.0685, 0.089,

0.026, and 0.017 across the parameters. The model's corresponding R^2 values were 0.893, 0.783, 0.873, and 0.763 for the respective parameter conditions.

Table 9 shows adsorption parameters calculated for adsorption of As(III) by the d adsorbent. At 298, 303, 308,

Table 9. Adsorption Parameters Calculated for Adsorption of As(III) by the d Adsorbent

model	parameters	298 K	303 K	308 K	313 K
Langmuir	q_m (μg/g)	1435	1323	1129	982
	K_L(L/μg)	0.005	0.005	0.007	0.004
	R^2	0.921	0.943	0.821	0.792
	R_L	0.22	0.31	0.26	0.29
Freundlich	K_F (L/μg)	534	298	189	148
	$1/n$	0.142	0.235	0.267	0.309
	R^2	0.933	0.964	0.952	0.912
Temkin	B (J/mol)	183.24	279.3	289.4	238.7
	K_T (L/μg)	0.043	0.067	0.058	0.086
	R^2	0.921	0.933	0.853	0.684

and 313 K, the Langmuir constants q_m were found to be 1435, 1323, 1129, and 982 μg/g, respectively. The Langmuir constants K_L for these temperatures were 0.005, 0.005, 0.007, and 0.004 L/μg. The coefficients of determination (R^2) for the Langmuir model at these temperatures were 0.921, 0.943, 0.821, and 0.792. The separation factor R_L values were 0.22, 0.31, 0.26, and 0.29 for the respective temperatures. For the Freundlich, the constants K_F at 298, 303, 308, and 313 K were 534, 298, 189, and 148 L/μg, respectively. The heterogeneity factor $1/n$ at these temperatures were 0.142, 0.235, 0.267, and 0.309. The R^2 values for the Freundlich model were 0.933, 0.964, 0.952, and 0.912. For the Temkin, the heat of adsorption constant B values at 298, 303, 308, and 313 K were 183.24, 279.3, 289.4, and 238.7 J/mol, respectively. The Temkin constants K_T were 0.043, 0.067, 0.058, and 0.086. The R^2 values for the Temkin model at these temperatures were 0.921, 0.933, 0.853, and 0.684.

3.7. Adsorption/Desorption Thermodynamics. In recent years, nanomaterials have been widely used in photocatalytic degradation, adsorption, and other fields.[39,40] To ascertain the significance of adsorption mechanisms, thermal parameters such as free energy of activation, heat, and entropy are crucial.[41] These were shown in the following equations:

$$\ln K = -\frac{\Delta H^0}{RT} + \frac{\Delta S^0}{R} \qquad (15)$$

$$\Delta G^0 = \Delta H^0 - T\Delta S^0 \qquad (16)$$

The adsorption process was an endothermic reaction. This reaction is nontransient at high temperatures and typically spontaneous. As was shown in the adsorption dynamics and adsorption thermodynamics, the unfavorable adsorption is driven by entropy. In addition, the four adsorbent sorptions do not spontaneously occur at high temperatures, indicating that the adsorption is thermally driven.

To examine the impact of the eluent on the desorption of As(III) from solid adsorption residues, a comprehensive desorption study was undertaken. Two distinct eluent systems were deployed: 0.5 M NaOH (pH = 13) and 0.5 M NaCl (pH = 6). Recent research indicates that NaCl outperforms NaOH as an eluent. However, due to the primary adsorption

mechanisms, particularly chemical adsorption and complex formation, the desorption of arsenic remains limited.

Furthermore, pH plays a vital role in desorption, with higher desorption percentages observed when pH shifts from alkaline to neutral and subsequently to acidic. It is worth noting that iron leaches into the desorption medium when magnetite is combined with a carbon medium. Given the influence of pH, NaCl is considered an excellent eluent.

Table 10 shows the thermodynamic parameters for adsorption of As(III) by different adsorbents. As shown in

Table 10. Thermodynamic Parameters for Adsorption of As(III) by Different Adsorbents

adsorbent	temperature (K)	ΔH(kJ/mol)	ΔS (J/Kmol)	ΔG(kJ/mol)
a	298	53.56	151.32	8.47
	303			7.71
	308			6.95
	313			6.20
b	298	−13.29	−83.73	11.61
	303			12.08
	308			12.50
	313			12.92
c	298	−74.53	−289.45	11.73
	303			13.17
	308			14.62
	313			16.07
d	298	−88.74	−332.23	10.26
	303			11.93
	308			13.59
	313			15.25

Table 10, for the *a* adsorbent, the ΔH was 53.56 kJ/mol, the ΔS was 151.32 J/Kmol, and the ΔG of 298, 303, 308, and 313 were 8.47, 7.71, 6.95, and 6.20 kJ/mol, respectively. For the *b* adsorbent, the ΔH was −13.29 kJ/mol, the ΔS was −83.73 J/Kmol, and the ΔG for 298, 303, 308, and 313 K were 11.61, 12.08, 12.50, and 12.92 kJ/mol, respectively. For the *c* adsorbent, the ΔH was −74.53 kJ/mol, the ΔS was −289.45 J/Kmol, and the ΔG for 298, 303, 308, and 313 K were 11.73, 13.17, 14.62, and 16.07 kJ/mol, respectively. For the *d* adsorbent, the ΔH was −88.74 kJ/mol, the ΔS was −332.23 J/Kmol, and the ΔG for 298, 303, 308, and 313 K were 10.26, 11.93, 13.59, and 15.25 kJ/mol, respectively.

4. CONCLUSIONS

In this study, the different As(III) adsorbents were synthesized and the results indicated the high As(III) removal efficiency. Previous studies often relied on basic activated carbon or other common adsorbents and primarily employed Freundlich or Temkin models for characterization. Our hydrothermally synthesized magnetically activated carbon showed unique adsorption kinetics that differ from existing literature, being best described by the pseudo-second-order and Langmuir models. The pore size distributions indicated that the corresponding pore distribution was uniform, and zeta potentials and TG analysis were used to measure the adsorbent-charged characteristics and thermostability. Different adsorbents of zeta potentials would decrease with the increase in pH. In addition, for different adsorbents *a*, *b*, *c*, and *d*, the corresponding adsorption capabilities were different. For the *a*, *b*, *c*, and *d* adsorbents, the pseudo-first-order model, the $q_{e\ (cal)}$ values for the four adsorbents were 434.2, 418.4, 283.5,

and 279.5 μg/g, respectively. Take adsorbent *a* as an example; the q_m values for 298, 303, 308, and 313 K were 702, 673, 605, and 589 μg/g, respectively, and K_L values of these temperatures were 0.021, 0.031, 0.018, and 0.009 L/μg, respectively. For the Langmuir model, the R^2 values at the four temperatures were 0.999, 0.978, 0.985, and 0.993, respectively, which indicated that the Langmuir model showed higher fitness. For the Freundlich model, the K_L values (L/μg) at parameters of these temperatures are 432, 409, 328, and 294, respectively. For the Freundlich model, the $1/n$ values at temperatures of 298, 303, 308, and 313 K are 0.049, 0.045, 0.052, and 0.035, respectively. For the Freundlich model, the R^2 values at parameters of 298, 303, 308, and 313 K are 0.986, 0.989, 0.982, and 0.872, respectively. For the Temkin model, the B values (J/mol) are 30.93, 0.894, 0.824, and 0.782 at these temperatures, respectively. The K_T values (in L/μg) are 1.02×10^6, 0.07×10^6, 0.003×10^6, and 0.002×10^6, respectively. The R^2 values are 0.973, 0.958, 0.972, and 0.894, respectively. In this study, the corresponding adsorption dynamics were fitted by the pseudo-first-order model, pseudo-second-order model, Elovich model, and intraparticle diffusion model, and different adsorbents showed different fitted parameters. In the end, the adsorption thermodynamics were fitted by different models, and the corresponding adsorption mechanism was explored. However, this paper lacked the molecular dynamics simulation section, and in the future, a detailed mechanism should be verified by molecular dynamics simulation.

■ AUTHOR INFORMATION

Corresponding Author

Hao Zhu − *Department of Stomatology, General Hospital of Northern Theater Command, Shenyang 110016, China;* ⓞ orcid.org/0009-0003-2480-3721; Email: zhuhaozhzh1234@163.com

Authors

Wenhui Lin − *School of Materials Science and Engineering, Shanghai Jiao Tong University, Shanghai 200030, China*

Liwen Fan − *College of Chemical and Biological Engineering, Zhejiang University, Hangzhou 310027, China*

Complete contact information is available at:
https://pubs.acs.org/10.1021/acsomega.3c03590

Notes

The authors declare no competing financial interest.

■ REFERENCES

(1) Zhuang, F.; Huang, J.; Li, H.; Peng, X.; Xia, L.; Zhou, L.; Zhang, T.; Liu, Z.; He, Q.; Luo, F.; Yin, H.; Meng, D. Biogeochemical behavior and pollution control of arsenic in mining areas: A review. *Front. Microbiol.* **2023**, *14*, 1043024 DOI: 10.3389/fmicb.2023.1043024.

(2) Ouyang, T.; Li, M.; Appel, E.; Tang, Z.; Peng, S.; Li, S.; Zhu, Z. Magnetic response of Arsenic pollution in a slag covered soil profile close to an abandoned tungsten mine, southern China. *Sci. Rep.* **2020**, *10* (1), 4357 DOI: 10.1038/s41598-020-61411-6.

(3) Le, D. V.; Giang, P. T. K.; Nguyen, V. T. Investigation of arsenic contamination in groundwater using hydride generation atomic absorption spectrometry. *Environ. Monit. Assess.* **2023**, *195* (1), 84 DOI: 10.1007/s10661-022-10707-3.

(4) Cinar, L.; Erdem, D. B. Evaluation of Arsenic status of soils around some wild storage areas in Thrace Region, Turkey. *Fresenius Environ. Bull.* **2020**, *29* (12A), 11342−11348.

(5) Gong, Y.; Qu, Y.; Yang, S.; Tao, S.; Shi, T.; Liu, Q.; Chen, Y.; Wu, Y.; Ma, J. Status of arsenic accumulation in agricultural soils across China (1985−2016). *Environ. Res.* **2020**, *186*, No. 109525.

(6) Omeroglu, E. E.; Sudagidan, M.; Ogun, E. Arsenic Pollution and Anaerobic Arsenic Metabolizing Bacteria in Lake Van, the World's Largest Soda Lake. *Life* **2022**, *12* (11), 1900 DOI: 10.3390/life12111900.

(7) Sun, M. L.; Wang, Z.; Ye, Y. F.; Wang, Q.; Ma, X. Y.; Zhao, Z. X. Review: Complexation mechanism of organic matter and arsenic on iron-containing minerals. *Environ. Geotech.* **2022**, *40*, 1.

(8) Zhu, Y.; Yang, Q.; Wang, H.; Yang, J.; Zhang, X.; Li, Z.; Martín, J. D. A hydrochemical and isotopic approach for source identification and health risk assessment of groundwater arsenic pollution in the central Yinchuan basin. *Environ. Res.* **2023**, *231*, No. 116153.

(9) Ghobadi, A.; Cheraghi, M.; Sobhanardakani, S.; Lorestani, B.; Merrikhpour, H. Hydrogeochemical characteristics, temporal, and spatial variations for evaluation of groundwater quality of Hamedan−Bahar Plain as a major agricultural region, West of Iran. *Environ. Earth Sci.* **2020**, *79* (18), 428 DOI: 10.1007/s12665-020-09177-y.

(10) Liu, C. C.; Jean, J. S.; Nath, B.; Lee, M. K.; Hor, L. I.; Lin, K. H.; Maity, J. P. Geochemical characteristics of the fluids and muds from two southern Taiwan mud volcanoes: Implications for water−sediment interaction and groundwater arsenic enrichment. *Appl. Geochem.* **2009**, *24* (9), 1793−1802.

(11) Dilpazeer, F.; Munir, M.; Baloch, M.; Shafiq, I.; Iqbal, J.; Saeed, M.; Abbas, M.; Shafique, S.; Aziz, K.; Mustafa, A.; Mahboob, I. A Comprehensive Review of the Latest Advancements in Controlling Arsenic Contaminants in Groundwater. *Water* **2023**, *15* (3), 478.

(12) Pathan, S.; Bose, S. Biopolymer based hydrogels for arsenic removal. *Curr. Sci.* **2020**, *118* (10), 1540−1546.

(13) Yin, S. H.; Yang, L. S.; Wen, Q. Q.; Wei, B. G. Temporal variation and mechanism of the geogenic arsenic concentrations in global groundwater. *Appl. Geochem.* **2022**, *146*, No. 105475.

(14) Rahnamarad, J.; Derakhshani, R.; Abbasnejad, A. Data on arsenic contamination in groundwater of Rafsanjan plain, Iran. *Data in Brief* **2020**, *31*, No. 105772.

(15) Gao, Z.; Guo, H.; Qiao, W.; Ke, T.; Zhu, Z.; Cao, Y.; Su, X.; Wan, L. Abundant Fe(III) Oxide-Bound Arsenic and Depleted Mn Oxides Facilitate Arsenic Enrichment in Groundwater From a Sand-Gravel Confined Aquifer. *J. Geophys. Res.-Biogeosci.* **2022**, *127* (8), No. e2022JG006942, DOI: 10.1029/2022JG006942.

(16) Ding, W.; Wan, X.; Zheng, H.; Wu, Y.; Muhammad, S. Sulfite-assisted oxidation/adsorption coupled with a TiO2 supported CuO composite for rapid arsenic removal: Performance and mechanistic studies. *J. Hazard. Mater.* **2021**, *413*, No. 125449.

(17) Cai, G. Y.; Li, L. P.; Li, D. K.; Wang, Q. Y.; Zhang, L. Y.; Zhang, J.; Zuo, W.; Tian, Y. Rapid purification of As(III) in water using iron−manganese composite oxide coupled with sulfite: Importance of the SO5·- radicals. *Water Res.* **2022**, *222*, No. 118839.

(18) Ding, W.; Zheng, H.; Sun, Y.; Zhao, Z.; Zheng, X.; Wu, Y.; Xiao, W. Activation of MnFe2O4 by sulfite for fast and efficient removal of arsenic (III) at circumneutral pH: Involvement of Mn(III). *J. Hazard. Mater.* **2021**, *403*, No. 123623.

(19) Katsoyiannis, I. A.; Zouboulis, A. I.; Jekel, M. Kinetics of bacterial As(III) oxidation and subsequent As(V) removal by sorption onto biogenic manganese oxides during groundwater treatment. *Ind. Eng. Chem. Res.* **2004**, *43* (2), 486−493.

(20) Meez, E.; Tolkou, A. K.; Giannakoudakis, D. A.; Katsoyiannis, I. A.; Kyzas, G. Z. Activated Carbons for Arsenic Removal from Natural Waters and Wastewaters: A Review. *Water* **2021**, *13* (21), 2982.

(21) Liu, Y.; Cai, L.; Wang, X.; Chen, Z.; Yang, W. Efficient adsorption of arsenic in groundwater by hydrated iron oxide and ferromanganese oxide chitosan gel beads. *Sep. Purif. Technol.* **2023**, *315*, No. 123692, DOI: 10.1016/j.seppur.2023.123692.

(22) Zaib, Q.; Masoumi, Z.; Aich, N.; Kyung, D. Review of the synthesis and applications of deep eutectic solvent-functionalized adsorbents for water treatment. *J. Environ. Chem. Eng.* **2023**, *11* (3), No. 110214.

(23) Fahad, S. A.; Nawab, M. S.; Shaida, M. A.; Verma, S.; Khan, M. U.; Siddiqui, V.; Naushad, M.; Saleem, L.; Farooqi, I. H. Carbon based adsorbents as efficient tools for the removal of U(VI) from aqueous medium: A state of the art review. *J. Water Process Eng.* **2023**, *52*, No. 103458.

(24) Eniola, J. O.; Sizirici, B.; Fseha, Y.; Shaheen, J. F.; Aboulella, A. M. Application of conventional and emerging low-cost adsorbents as sustainable materials for removal of contaminants from water. *Environ. Sci. Pollut. Res.* **2023**, *30*, 88245−88271.

(25) Chen, C. K.; Nguyen, N. T.; Le, T. T.; Duong, C. C.; Nguyen, C. N.; Truong, D. T.; Liao, C. H. Novel design of amine and metal hydroxide functional group modified onto sludge biochar for arsenic removal. *Water Sci. Technol.* **2022**, *85* (5), 1384−1399.

(26) Alka, S.; Shahir, S.; Ibrahim, N.; Ndejiko, M. J.; Vo, D. V. N.; Manan, F. A. Arsenic removal technologies and future trends: A mini review. *J. Cleaner Prod.* **2021**, *278*, No. 123805, DOI: 10.1016/j.jclepro.2020.123805.

(27) Zang, S.; Zhang, R.; Lv, M.; Li, Y.; Zhou, H. Adsorption Technology and Mechanism of Roxarsone and Arsenic(V) Combined Pollution in Wastewater by Modified Plant Ash Biochar. *Russ. J. Phys. Chem. A* **2023**, *97* (1), 248−256.

(28) Mostafapour, F. K.; Radmehr, M.; Siddiqi, S. H.; Balarak, D. Evaluation of Sono-photocatalytic Removal of Ciprofloxacin Antibiotic Using Magnesium Oxide Nanoparticles from Aqueous Solutions. *Int. J. Pharm. Invest.* **2023**, *13* (2), 238−242.

(29) Al-Musawi, T. J.; Yilmaz, M.; Mohebi, S.; Balarak, D. Ultraviolet radiation/persulfate/hydrogen peroxide treatment system for the degradation of acid blue 80 dye from a batch flow chemical reactor: effects of operational parameters, mineralization, energy consumption, and kinetic studies. *Energy Ecol. Environ.* **2022**, *7* (6), 630−640.

(30) Fan, Z.; Zhang, Q.; Li, M.; Sang, W.; Qiu, Y.; Wei, X.; Hao, H. Removal behavior and mechanisms of Cd(II) by a novel MnS loaded functional biochar: Influence of oxygenation. *J. Cleaner Prod.* **2020**, *256*, No. 120672.

(31) Cantuaria, M. L.; Nascimento, E. S.; Neto, A. F. A.; dos Santos, O. A. A.; Vieira, M. G. A. Removal and Recovery of Silver by Dynamic Adsorption on Bentonite Clay Using a Fixed-Bed Column System. *Adsorpt. Sci. Technol.* **2015**, *33* (2), 91−103.

(32) Qi, F. F.; Cao, Y.; Wang, M.; Rong, F.; Xu, Q. Nylon 6 electrospun nanofibers mat as effective sorbent for the removal of estrogens: kinetic and thermodynamic studies. *Nanoscale Res. Lett.* **2014**, *9*, 353 DOI: 10.1186/1556-276X-9-353.

(33) Wang, J.; Guo, X. Adsorption isotherm models: Classification, physical meaning, application and solving method. *Chemosphere* **2020**, *258*, No. 127279.

(34) Petkovska, M. Discrimination between adsorption isotherm models based on nonlinear frequency response results. *Adsorption* **2014**, *20* (2−3), 385−395.

(35) Chakraborty, A.; Sun, B. An adsorption isotherm equation for multi-types adsorption with thermodynamic correctness. *Appl. Therm. Eng.* **2014**, *72* (2), 190−199.

(36) Mostafapour, F. K.; Yilmaz, M.; Mahvi, A. H.; Younesi, A.; Ganji, F.; Balarak, D. Adsorptive removal of tetracycline from aqueous solution by surfactant-modified zeolite: equilibrium, kinetics and thermodynamics. *Desalin. Water Treat.* **2022**, *247*, 216−228.

(37) Kord Mostafapour, F.; Zolghadr, R.; Khodadadi Saloot, M.; Mahvi, A. H.; Balarak, D.; Safari, E. Removal of Acid blue 113 from aqueous medium using a novel magnetic adsorbent derived from activated carbon fiber. *Int. J. Environ. Anal. Chem.* **2022**, 1−16, DOI: 10.1080/03067319.2022.2130061.

(38) Al-Musawi, T. J.; Almajidi, Y. Q.; Al-Essa, E. M.; Romero-Parra, R. M.; Alwaily, E. R.; Mengelizadeh, N.; Ganji, F.; Balarak, D. Levofloxacin Adsorption onto MWCNTs/CoFe2O4 Nanocompo-

sites: Mechanism, and Modeling Using Non-Linear Kinetics and Isotherm Equations. *Magnetochemistry* **2023**, *9* (1), 9.

(39) Rajiv, P.; Mengelizadeh, N.; McKay, G.; Balarak, D. Photocatalytic degradation of ciprofloxacin with Fe2O3 nanoparticles loaded on graphitic carbon nitride: mineralisation, degradation mechanism and toxicity assessment. *Int. J. Environ. Anal. Chem.* **2023**, *103* (10), 2193−2207.

(40) Al-Musawi, T. J.; Mengelizadeh, N.; Alwared, A. I.; Balarak, D.; Sabaghi, R. Photocatalytic degradation of ciprofloxacin by MMT/CuFe2O4 nanocomposite: characteristics, response surface methodology, and toxicity analyses. *Environ. Sci. Pollut. Res.* **2023**, *30* (27), 70076−70093.

(41) Sillanpaa, M.; Mahvi, A. H.; Balarak, D.; Khatibi, A. D. Adsorption of Acid orange 7 dyes from aqueous solution using Polypyrrole/nanosilica composite: Experimental and modelling. *Int. J. Environ. Anal. Chem.* **2023**, *103* (1), 212−229.